Atom-counting in High Resolution Electron Microscopy
TEM or STEM – That's the question

Gonnissen, J.; De Backer, A.; den Dekker, A. J.; Sijbers, J.; Van Aert, S.

DOI
10.1016/j.ultramic.2016.10.011

Publication date
2017

Document Version
Accepted author manuscript

Published in
Ultramicroscopy

Citation (APA)
Gonnissen, J., De Backer, A., den Dekker, A. J., Sijbers, J., & Van Aert, S. (2017). Atom-counting in High Resolution Electron Microscopy: TEM or STEM – That's the question. *Ultramicroscopy*, *174*, 112-120. https://doi.org/10.1016/j.ultramic.2016.10.011

Link to formal publication in Ultramicroscopy (Elsevier): https://doi.org/10.1016/j.ultramic.2016.10.011

Atom-counting in High Resolution Electron Microscopy: TEM or STEM - that's the question

J. Gonnissen[a], A. De Backer[a], A.J. den Dekker[b,c], J. Sijbers[b], S. Van Aert[a,*]

[a] *Electron Microscopy for Materials Science (EMAT), University of Antwerp, Groenenborgerlaan 171, 2020 Antwerp, Belgium*
[b] *iMinds-Vision Lab, University of Antwerp, Universiteitsplein 1, 2610 Wilrijk, Belgium*
[c] *Delft Center for Systems and Control (DCSC), Delft University of Technology, Mekelweg 2, 2628 CD Delft, The Netherlands*

Abstract

In this work, a recently developed quantitative approach based on the principles of detection theory is used in order to determine the possibilities and limitations of High Resolution Scanning Transmission Electron Microscopy (HR STEM) and HR TEM for atom-counting. So far, HR STEM has been shown to be an appropriate imaging mode to count the number of atoms in a projected atomic column. Recently, it has been demonstrated that HR TEM, when using negative spherical aberration imaging, is suitable for atom-counting as well. The capabilities of both imaging techniques are investigated and compared using the probability of error as a criterion. It is shown that for the same incoming electron dose, HR STEM outperforms HR TEM under common practice standards, i.e. when the decision is based on the probability function of the peak intensities in HR TEM and of the scattering cross-sections in HR STEM. If the atom-counting decision is based on the joint probability function of the image pixel values, the dependence of all image pixel intensities as a function of thickness should be known accurately. Under this assumption, the probability of error may decrease significantly for atom-counting in HR TEM and may, in theory, become lower as compared to HR STEM under the predicted optimal experimental settings. However, the commonly used standard for atom-counting in HR STEM leads to a high performance and has been shown to work in practice.

Keywords: High-resolution (scanning) transmission electron microscopy (HR (S)TEM), Electron microscope design and characterisation, Data processing/image processing

1. Introduction

In modern technology, nanoparticles play an important role because of their unique properties, which are determined by their 3D atomic structure. The quest to find new materials with improved applications has therefore driven research the past few years to develop methods to characterise nanostructures in three dimensions with highest precision. Significant advances have been made in quantitative electron microscopy, for example, by combining annular dark field (ADF) STEM with atom-counting [1–4]. Based on the retrieved atom-counting results, the 3D atomic structure of a nanoparticle can then be reconstructed using discrete tomography [1]. So far, ADF STEM images have been used for atom-counting together with advanced statistical techniques [1–5]. LeBeau *et al.* [6] and Jones *et al.* [7] compared simulated atom column intensities with normalised experimentally measured atom column intensities in order to count the number of atoms from HR STEM images. For atom-counting, one needs a performance measure that enables to distinguish between different numbers of atoms. In previous work, it was shown that the total intensity of scattered electrons, the so-called scattering cross-section (SCS) is an appropriate measure for atom-counting [1, 5, 8, 9]. The SCS is a more robust measure as compared to the peak intensity (PI), since it is much less affected by a small mistilt of the sample, the defocus, source coherence and other residual aberrations [10, 11]. In HR TEM, it has been shown that the number of atoms in a projected atomic column can be counted using negative spherical aberration imaging [12]. In [12], atoms were counted from HR TEM image PIs of a thin MgO crystal.

Ultimately, the pixel values in a HR (S)TEM image are Poisson distributed because of the presence of in-

*Corresponding author
Email address: sandra.vanaert@uantwerpen.be (S. Van Aert)
[1] *Phone*: +32 3 2653252

herent counting noise, which sets fundamental limits to the precision with which the number of atoms can be determined. A quantitative approach based on the principles of detection theory was developed, in order to optimise the experiment design for the detection of light atoms [13–15]. In this work, this quantitative approach is used to investigate the capabilities of HR TEM and HR STEM for atom-counting. In statistical detection theory, the so-called probability of error, P_e, can be calculated as a function of the experimental parameters when comparing two or more hypotheses using a binary or multiple hypothesis test, respectively. For the atom-counting problem, the hypotheses correspond to different possible column thicknesses [9]. For the computation of this probability to miscount the number of atoms, realistic simulations describing the experimental images can be used [16–21], together with knowledge about the statistics of the image pixel values. The experimental settings leading to the lowest probability to miscount the number of atoms then correspond to the optimal experiment design for atom-counting. To compare the probability of error for both HR TEM and HR STEM, simulations are performed for a thin MgO crystal, as well as for a thicker $SrTiO_3$ crystal and a heavier Au crystal for varying experimental settings in both imaging modes.

The paper is organised as follows: statistical detection theory is discussed and the probability of error for atom-counting is introduced in Section 2. In Section 3, the procedure to optimise the experiment design is explained and discussed using the probability of error as the optimality criterion, both for HR TEM and HR STEM. First, a comparison is made when decision rules are derived using the probability function (PF) of the PIs and SCSs in HR TEM and HR STEM, respectively. In a second step, the image intensities in both imaging modes are compared on a pixel by pixel basis, where the atom-counting decision is based on the *joint* PF of the image pixel values. The results of the obtained optimal experiment designs are discussed in Section 4, and in Section 5 conclusions are drawn.

2. Statistical detection theory

In the case where one needs to decide if there are n or $n+1$ atoms in a projected atomic column, one can translate this problem into a binary hypothesis test with hypotheses [22]:

$$\begin{aligned} \mathcal{H}_0 &: n_{\mathcal{H}_0} = n \\ \mathcal{H}_1 &: n_{\mathcal{H}_1} = n+1, \end{aligned} \tag{1}$$

where $\mathcal{H}_0$ is referred to as the null hypothesis, $\mathcal{H}_1$ as the alternative hypothesis and $n_{\mathcal{H}_i}$ denotes the number of atoms under hypothesis $\mathcal{H}_i$. The theory for binary hypothesis testing was derived in [13, 14] for the detection of light atoms. However, a binary hypothesis test is no longer adequate if the corresponding probabilities of error lead to different designs for different choices of the two hypotheses. Therefore, the approach of binary hypothesis testing was extended in [9] towards multiple hypothesis testing for atom-counting. For readability of this work, the theoretical background is summarised here.

Suppose we want to decide among M possible hypotheses:

$$\{\mathcal{H}_0, \mathcal{H}_1, \ldots, \mathcal{H}_{M-1}\}. \tag{2}$$

For atom-counting, the number of hypotheses typically equals the maximum number of atoms in a column which should be considered for the sample under study. The decision rule is now defined such that the probability of error is minimised. The minimum probability of error decision rule is then to decide $\mathcal{H}_k$ if

$$p_{\mathbf{w}}(\mathbf{w}|\mathcal{H}_k)P(\mathcal{H}_k) > p_{\mathbf{w}}(\mathbf{w}|\mathcal{H}_i)P(\mathcal{H}_i) \quad \forall i \neq k. \tag{3}$$

This decision rule is termed the *maximum a posteriori probability* (MAP) decision rule [22]. In this expression, $p_{\mathbf{w}}(\mathbf{w}|\mathcal{H}_i)$ is the conditional (joint) probability (density) function (P(D)F) $p_{\mathbf{w}}(\boldsymbol{\omega}|\mathcal{H}_i)$ assuming $\mathcal{H}_i$ to be true, evaluated at the available observations $\mathbf{w}$. For equal prior probabilities $P(\mathcal{H}_i) = 1/M$, the decision rule given in Eq. (3) simplifies to

$$p_{\mathbf{w}}(\mathbf{w}|\mathcal{H}_k) > p_{\mathbf{w}}(\mathbf{w}|\mathcal{H}_i) \quad \forall i \neq k. \tag{4}$$

The exact expression for the PF $p_{\mathbf{w}}(\boldsymbol{\omega}|\mathcal{H}_i)$ was given and discussed in [9] for three different measures that can be used: HR (S)TEM images of a projected atomic column, PIs and SCSs. In this study, the variable $\boldsymbol{\omega}$ will take a different form for these three measures:

$$\begin{aligned} \boldsymbol{\omega}^{Im} &= [\omega_{11}, \omega_{12}, \omega_{21}, ..., \omega_{KL}]^T && \text{for (S)TEM images,} \\ \omega^{CS} &= \sum_{k=1}^{K}\sum_{l=1}^{L} \omega_{kl} \cdot (\Delta x)^2 && \text{for SCSs in STEM,} \\ \omega^{PI} & && \text{for PIs in TEM,} \end{aligned} \tag{5}$$

where the parameter ω_{kl} corresponds to the variables describing the pixel intensities of the HR (S)TEM image of the atomic column, Δx equals the pixel size, and ω^{PI} corresponds to the variable describing the pixel intensity at the position of the atomic column in a HR TEM

image. The index kl refers to the x- and y-coordinates $(x_k, y_l)^T$ of a set of KL pixel observations, which corresponds to the position of the probe in the case of HR STEM. Here, the atomic column positions were assumed to be known and correspond to a single pixel in the image. Based on the definition of ω^{PI}, it is clear that when using PIs one only takes the information of a single pixel into account. On the other hand, the detailed profiles of the images of atomic columns are represented in the multi-dimensional variable $\boldsymbol{\omega}^{Im}$. The SCS sums the pixel values in a Voronoi cell in the image, which are contained in $\boldsymbol{\omega}^{Im}$, into a single number, as defined by ω^{CS} in Eq. (5). For a binary hypothesis test, it was shown in [9] that the probability of error for SCSs almost equals the probability of error for the image intensities when the decision is based on the joint PF of the image pixel values. In the present paper, all three performance measures are compared in the case of multiple hypothesis testing.

In the case of a multiple hypothesis test, the probability of error is defined in the following way:

$$\mathrm{P_e} = \sum_{i=0}^{M-1} \sum_{j=0}^{M-1} C_{ij} P(\mathcal{H}_i|\mathcal{H}_j) P(\mathcal{H}_j), \tag{6}$$

where $P(\mathcal{H}_i|\mathcal{H}_j)$ is the conditional probability of deciding $\mathcal{H}_i$ when $\mathcal{H}_j$ is true, and

$$C_{ij} = \begin{cases} 1 & i \neq j \\ 0 & i = j \end{cases}. \tag{7}$$

The number of terms for the calculation of the probability of error used in Eq. (6) equals $M(M-1)$. Therefore, it is more efficient to calculate $\mathrm{P_c} = 1 - \mathrm{P_e}$, where $\mathrm{P_c}$ is the probability of a correct decision. In this case, the number of terms in the summation reduces to M:

$$\mathrm{P_c} = \sum_{i=0}^{M-1} P(\mathcal{H}_i|\mathcal{H}_i) P(\mathcal{H}_i), \tag{8}$$

where $P(\mathcal{H}_i|\mathcal{H}_i)$ corresponds to the probability that hypothesis $\mathcal{H}_i$ is decided assuming this hypothesis to be correct, and this is weighted by its prior probability $P(\mathcal{H}_i)$. This expression will now be calculated analytically; (1) for SCSs in HR STEM and (2) for PIs in HR TEM. In fact, since the pixel values of a HR (S)TEM image are considered as statistically independent electron counts, which are modelled as a Poisson distribution, their conditional PFs are well-known [9]. Since SCSs are defined by summing over the pixel values in a Voronoi cell of the atomic column, multiplied by the pixel area, they can also be described by using the Poisson distribution as explained in [9]. For equal prior probabilities $P(\mathcal{H}_i) = 1/M$, the probability of a correct decision for SCSs then corresponds to:

$$\begin{aligned} \mathrm{P_c} = \frac{1}{M} \Bigg[& F\left(\frac{x^{CS_{0,1}}}{(\Delta x)^2}, \lambda_{\mathcal{H}_0^s}\right) + \\ & F\left(\frac{x^{CS_{1,2}}}{(\Delta x)^2}, \lambda_{\mathcal{H}_1^s}\right) - F\left(\frac{x^{CS_{1,0}}}{(\Delta x)^2}, \lambda_{\mathcal{H}_1^s}\right) + \\ & F\left(\frac{x^{CS_{2,3}}}{(\Delta x)^2}, \lambda_{\mathcal{H}_2^s}\right) - F\left(\frac{x^{CS_{2,1}}}{(\Delta x)^2}, \lambda_{\mathcal{H}_2^s}\right) + \\ & \ldots + \\ & \left(1 - F\left(\frac{x^{CS_{M-1,M-2}}}{(\Delta x)^2}, \lambda_{\mathcal{H}_{M-1}^s}\right)\right)\Bigg], \end{aligned} \tag{9}$$

where $\mathcal{H}_i^s$ denotes the sorted hypotheses according to the expected values of the SCSs, and $x^{CS_{i,j}} = x^{CS_{j,i}}$ corresponds to the intersection between two neighbouring PFs. This intersection is given by

$$x^{CS_{i,j}} = \frac{\left(\lambda_{\mathcal{H}_i^s} - \lambda_{\mathcal{H}_j^s}\right)(\Delta x)^2}{\ln \frac{\lambda_{\mathcal{H}_i^s}}{\lambda_{\mathcal{H}_j^s}}}. \tag{10}$$

In this expression, $\lambda_{\mathcal{H}_i^s} = \sum_{k=1}^{K} \sum_{l=1}^{L} \lambda_{\mathcal{H}_i^s,kl}$ equals the sum over the expected values of the pixel intensities in a Voronoi cell of the atomic column, and $F\left(\frac{x^{CS_{i,j}}}{(\Delta x)^2}, \lambda_{\mathcal{H}_i^s}\right)$ is the Poisson cumulative distribution function with parameter $\lambda_{\mathcal{H}_i^s}$ evaluated at $x^{CS_{i,j}}/(\Delta x)^2$. The expected pixel intensities $\lambda_{\mathcal{H}_i^s,kl}$ can in practice be simulated using software for (S)TEM image simulations [17, 20]. A similar expression for the probability of a correct decision can be found for PIs, which can be used for atom-counting in HR TEM:

$$\begin{aligned} \mathrm{P_c} = \frac{1}{M} \Big[& F\left(x^{PI_{0,1}}, \lambda_{\mathcal{H}_0^s}\right) + \\ & F\left(x^{PI_{1,2}}, \lambda_{\mathcal{H}_1^s}\right) - F\left(x^{PI_{1,0}}, \lambda_{\mathcal{H}_1^s}\right) + \\ & F\left(x^{PI_{2,3}}, \lambda_{\mathcal{H}_2^s}\right) - F\left(x^{PI_{2,1}}, \lambda_{\mathcal{H}_2^s}\right) + \\ & \ldots + \\ & \left(1 - F\left(x^{PI_{M-1,M-2}}, \lambda_{\mathcal{H}_{M-1}^s}\right)\right)\Big], \end{aligned} \tag{11}$$

where the intersection between the different PFs is now given by

$$x^{PI_{i,j}} = \frac{\left(\lambda_{\mathcal{H}_i^s} - \lambda_{\mathcal{H}_j^s}\right)}{\ln \frac{\lambda_{\mathcal{H}_i^s}}{\lambda_{\mathcal{H}_j^s}}}, \tag{12}$$

and $\lambda_{\mathcal{H}_i^s}$ corresponds to $\lambda_{\mathcal{H}_i^s,PI}$, the expected pixel value at the atomic column position. It can be shown that for a multiple hypothesis test with M different hypotheses the maximum possible probability of error, for

which the correct hypothesis can not be decided, equals $(M-1)/M$.
When a decision is based on the joint PF of the image pixel values, which are defined by $\boldsymbol{\omega}^{Im}$ in Eq. (5), the probability of error given by Eq. (6), can not be calculated analytically anymore. In that case, the probability of error can only approximately be calculated using repetitive noise realisations, which is computationally intensive. By using the decision rule given by Eq. (4), the probability of error is then given by the fraction of miscounted numbers of atoms from a large set of noise realisations.

3. Optimal experiment design

The probability of error, given by Eq. (6) can be calculated as a function of the experimental settings and therefore be used to optimise the experiment design, as shown in [9, 13–15] for HR STEM applications. The optimal experiment design corresponds to the experimental settings that minimise the probability of error $\mathrm{P_e}$, or in other words maximise the probability on a correct atom-counting decision, $\mathrm{P_c}$. In a first comparison between both imaging techniques, the atom-counting decision was either based on the PF of the PIs for HR TEM as proposed in [12], or on the PF of the SCSs for HR STEM as suggested in [1, 5, 7–9]. After comparing both currently used methods, it was interesting to compare with the 'ultimate' situation using all image intensities on a pixel by pixel basis, although this would require a much more complex atom-counting procedure. In the comparison between HR TEM and HR STEM the incoming electron dose, $N(e^-/\text{Å}^2)$, was kept the same as it is a limiting factor in both imaging modes. Certainly if one wants to count the number of atoms from a HR (S)TEM image of a beam-sensitive material, the dose is a critical parameter that limits the atom-counting performance. In HR STEM, the incoming electron dose per probe position corresponds to $D_{STEM} = N \cdot (\Delta x)^2$ with Δx the pixel size, while in HR TEM, the total number of incident electrons is $D_{TEM} = N \cdot FOV$ with FOV the field of view. The expected pixel intensity values in HR TEM and HR STEM are therefore given by

$$\lambda^{TEM}_{\mathcal{H}_i,kl} = p_{kl,TEM} \cdot D_{TEM} \quad \text{and}$$
$$\lambda^{STEM}_{\mathcal{H}_i,kl} = p_{kl,STEM} \cdot D_{STEM} \quad \text{respectively,}$$

with

$$p_{kl,TEM} = \frac{I_{kl}}{\sum_{k=1}^{K}\sum_{l=1}^{L} I_{kl}} \quad \text{and}$$
$$p_{kl,STEM} = I_{kl},$$

corresponding to the probability that an electron hits a pixel (k,l) in a TEM or STEM experiment, respectively. In these expressions, I_{kl} is the intensity at pixel (k,l) which can be obtained using software that allows one to simulate (S)TEM images. In this work, the STEMsim software developed by A. Rosenauer was used [17].

3.1. Simulation parameters

An elaborate simulation study was performed for three investigated crystals: MgO, $SrTiO_3$ and Au. In the case of HR TEM, the spherical aberration (C_s) and defocus (ε) were considered as the most influencing experimental parameters, while for HR STEM the inner and outer detector angles of the annular STEM detector were assumed to affect the atom-counting performance the most. The experiment design was therefore optimised by computing the probability of error as a function of either spherical aberration and defocus, or inner and outer detector angle for HR TEM and HR STEM, respectively. The optimal experiment design then corresponds to the settings that minimise the probability of error. Absorptive potential multislice calculations were used to simulate the HR STEM images, using settings for an aberration-corrected microscope under Scherzer defocus, for a whole range of annular STEM detector rings. Frozen lattice calculations were performed for the HR TEM image simulations, using the phase contrast transfer function for partially coherent imaging [23, 24], for a whole range of spherical aberration and defocus values. The used simulation parameters are listed in Table 1 for MgO, $SrTiO_3$ and Au.

3.2. Results for peak intensities and scattering cross-sections

The optimal experiment design was investigated for realistic simulation experiments, using the analytical expressions for the probability of error for atom-counting in HR TEM and HR STEM, given by Eq. (6). In this section, the probability of error was calculated when the decision was based on the PF of the SCSs in HR STEM, and on the PF of the PIs in HR TEM, for which the probabilities for a correct decision are given by Eqs. (9) and (11), respectively. Therefore, a first elaborate simulation study of MgO was performed for counting up to 12 atoms (i.e. 6 unit cells) corresponding to a column thickness of 2.5 nm, like in [12]. The probability of error for atom-counting was then calculated as a function of the experimental parameters for PIs in HR TEM and SCSs in HR STEM, for incoming electron doses of $10^4 e^-/\text{Å}^2$ and $10^7 e^-/\text{Å}^2$. Results of the probability of error for PIs in HR TEM are shown

	Symbol	MgO	$SrTiO_3$	Au
General parameters				
Debye-Waller factor	B (Å^2)	B_{Mg}= 0.30 B_O = 0.34	B_{Sr} = 0.6214 B_{Ti} = 0.4398 B_O = 0.7323	B_{Au} = 0.6198
Zone orientation	[uvw]	[001]	[100]	[001]
Acceleration voltage	V (kV)	300	300	300
Size of the supercell	$N_a \times N_b$ (nm^2)	3.8×3.8	4.3×4.3	3.3×3.3
STEM parameters				
Slice thickness	z_{slice} (Å)	2.106	1.95	2.0391
Defocus	ε (Å)	-83.01	-14.03	-83.01
Spherical aberration	C_s (mm)	0.001	0.001	0.001
Spherical aberration of 5th order	C_5 (mm)	0	0	0
Semi-convergence angle	α (mrad)	21.7	20	21.7
Pixel size	Δx (Å)	0.2106	0.1562	0.20391
FWHM of the source image	$FWHM_s$ (Å)	0.7	0.7	0.7
Number of pixels in the unit cell	$K \times L$	20×20	25×25	20×20
TEM parameters				
Number of FP configurations	N	7×7×4×30	9×9×4×30	7×7×4×30
Pixel size	Δx (Å)	0.0165	0.046488	0.03186
Number of pixels in the unit cell	$K \times L$	256×256	84×84	128×128

Table 1: Parameter values used for the STEM and TEM simulations of MgO, $SrTiO_3$ and Au.

in Fig. 1(a) and 1(b). From these figures, it is clear that for the investigated values for the spherical aberration and defocus, P_e reaches high values for the incoming electron dose of $N = 10^4 e^-/Å^2$, while it is substantially lower for $N = 10^7 e^-/Å^2$. In Fig. 1(a), the result for the lower incoming electron dose of $10^4 e^-/Å^2$ is presented, where P_e is minimal for the setting $C_s = -0.025$ mm and $\varepsilon = 57$Å. For this setting, however, the probability to miscount the number of atoms is high and equals 66%. For the higher incoming electron dose of $10^7 e^-/Å^2$, there is a large dark-blue region visible in Fig. 1(b) corresponding to a very low probability of error, that is optimal for atom-counting in HR TEM. For this electron dose P_e is minimised and close to 0 for the setting $C_s = -0.025$ mm and $\varepsilon = 49$Å. As expected, this indicates that the atom-counting precision becomes much better for a higher incoming electron dose.
Results of P_e when the decision was based on the PF of the SCSs in HR STEM are shown in Figs. 1(c) and 1(d), for the same two incoming electron doses that were used for HR TEM. A clear optimal detector range is obtained for both incoming electron doses in the Annular Bright Field (ABF) STEM regime for a detector range of $13 - 20$ mrad, visible as the dark-blue region where the probability of error is close to 0. Local optima are also found in the Low Angle ADF (LAADF) STEM regime for both incoming electron doses, as well as in the BF regime ($0 - 10$ mrad) where the probability of error is about 10%. It can be seen that P_e for atom-counting is much lower for HR STEM as compared to HR TEM, even for a low incoming electron dose.

Next, an elaborate simulation study for a $SrTiO_3$ crystal was performed for a thickness up to 75 atoms, corresponding to a column thickness of about 30 nm. The results for P_e for atom-counting from HR TEM and HR STEM are shown in Fig. 2 for the Sr column in $SrTiO_3$. In this figure, decision rules were again based on the PFs of the performance measures that currently have been used in practice, i.e. the PIs and SCSs for HR TEM and HR STEM, respectively. Based on the results shown in Fig. 2, it is clear that P_e for atom-counting in HR TEM is high as compared to HR STEM. In HR TEM, P_e is minimised for the setting $C_s = -0.035$ mm and $\varepsilon = -80$Å. However, for this setting the probability to miscount the number of atoms is still high and equals 48%. In HR STEM, for a thickness of 75 atoms, the

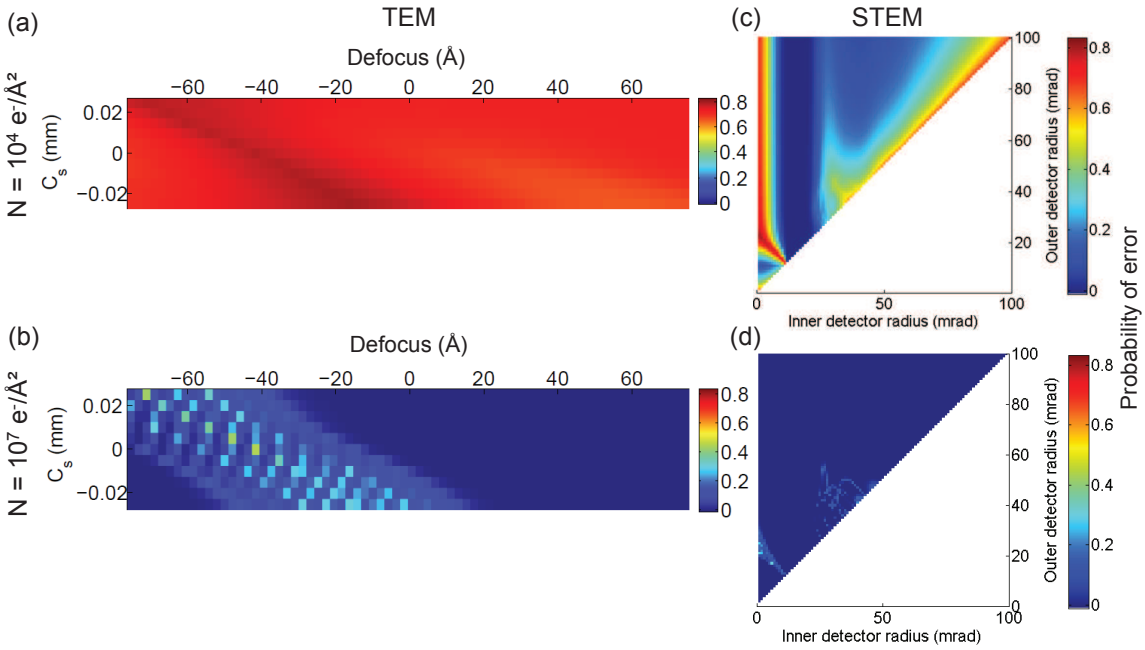

Figure 1: P_e for atom-counting using PI in HR TEM (a and b) and SCS in HR STEM (c and d) for a MgO column up to 12 atoms thick, for $N = 10^4 e^-/\text{Å}^2$ (a and c) and $N = 10^7 e^-/\text{Å}^2$ (b and d).

optimal detector range that minimises P_e equals 27-100 mrad, for which the probability of error is 0.5%. For a probe semi-convergence angle of 21.7 mrad, this optimal detector design corresponds to LAADF STEM.

3.3. Results for image intensities on a pixel by pixel basis

So far, two currently used methods for atom-counting were compared, but in this section, the 'ultimate' situation when the decision is based on the joint PF of the image pixel values was investigated. Although this requires a more complex framework, it was interesting to investigate and compare the limits of both imaging techniques in this case. As was mentioned before, Eq. (6) can only be computed approximately following the decision rule given in Eq. (4) using multiple noise realisations, when the atom-counting decision is based on the joint PF of the image pixel values. The experimental parameters were varied and optimised in the same way as before, for an incoming electron dose of $10^4 e^-/\text{Å}^2$. Results for PF's of PIs and SCSs were compared with results when using all image intensities on a pixel by pixel basis for a Sr column in $SrTiO_3$ up to 30 atoms thick, as well as for a heavier Au column up to 50 atoms thick. Results of the probability of error for atom-counting in HR TEM and HR STEM are shown in Fig. 3 for the Sr column and in Fig. 4 for the Au column, for the different performance measures.

When comparing Fig. 3(a) and 3(b), it is evident that the probability of error decreases significantly when the decision is based on the joint PF of all HR TEM image pixel values, as compared to the result based on the PF of the PIs. For HR STEM, there is only a slight decrease in probability of error, which can be seen when comparing Figs. 3(c) and 3(d). For the Au column, similar results were found which are presented in Figs. 4(c) and 4(d). In [9], it was already shown for a binary hypothesis test that the probability of error for the SCSs approximately equals the probability of error when using all image intensities on a pixel by pixel basis. From the results shown here, it can be seen that this is also true for a multiple hypothesis test.

4. Discussion

4.1. Results for peak intensities and scattering cross-sections

The difference in probability of error between HR TEM and HR STEM for the MgO column, of which the results are shown in Fig. 1, can be understood by investigating the performance measures as a function of thickness. In Fig. 5, both the PIs for HR TEM and

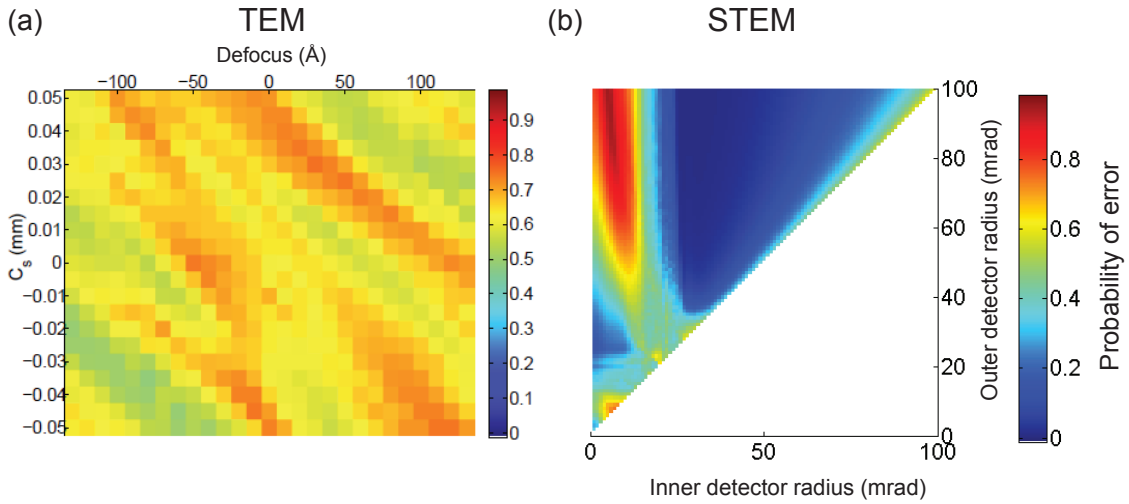

Figure 2: P_e for atom-counting using (a) PIs in HR TEM and (b) SCSs in HR STEM for a Sr column with a thickness up to 75 atoms and $N = 10^6 e^-/\text{Å}^2$.

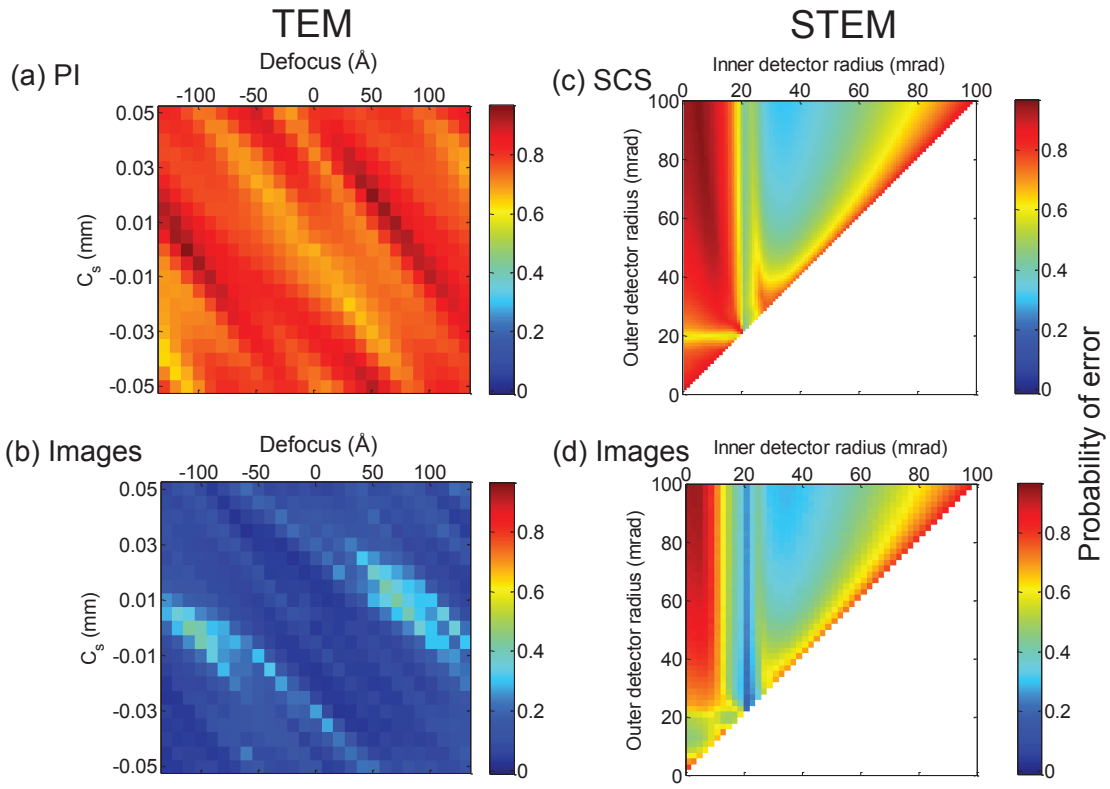

Figure 3: P_e for atom-counting using (a) PIs in HR TEM, (b) image intensities on a pixel by pixel basis in HR TEM, or (c) SCSs in HR STEM and (d) image intensities on a pixel by pixel basis in HR STEM, for a Sr column with a thickness up to 30 atoms, and $N = 10^4 e^-/\text{Å}^2$.

the SCSs for HR STEM are plotted as a function of the number of atoms, at the optimal experimental settings. From the results shown in Fig. 5, it can be seen that both the PIs and the SCSs increase almost linearly with the

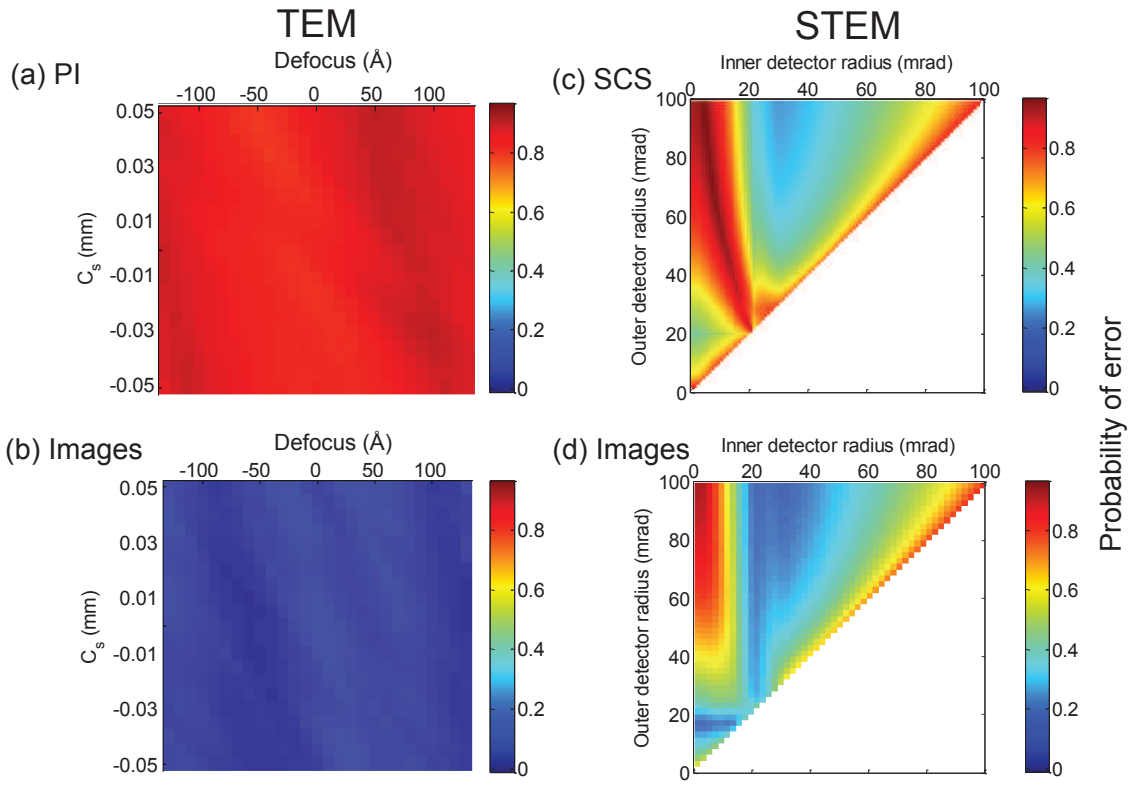

Figure 4: P_e for atom-counting using (a) PIs in HR TEM, (b) image intensities on a pixel by pixel basis in HR TEM, or (c) SCSs in HR STEM and (d) image intensities on a pixel by pixel basis in HR STEM, for a Au column with a thickness up to 50 atoms, and $N = 10^4 e^-/\text{Å}^2$.

thickness under the optimal settings, which allows us to distinguish between different numbers of atoms. However, in Fig. 1, a much lower probability of error was obtained for atom-counting in HR STEM as compared to HR TEM. This can be understood by looking at the succeeding PFs of the respective performance measures for the different column thicknesses, which are presented in Fig. 6. In Fig. 6(a), it is shown that the difference between the mean values of the PFs of consecutive PIs is small as compared to their standard deviation at the lower incoming electron dose of $10^4 e^-/\text{Å}^2$, which results in highly overlapping PFs. The large overlap results in a high probability of error, which makes it hard to distinguish between the different column thicknesses in the case of HR TEM. In Fig. 6(b) and 6(d), it is visible that the precision of the SCSs and PIs improves significantly with the incoming electron dose. Therefore, a higher incoming electron dose decreases the probability of error both in HR TEM and HR STEM. For HR STEM at the lower incoming electron dose, the difference between the mean values of the PFs of consecutive SCS values was already large as compared to their standard deviation, which follows from Fig. 6(c). The different column thicknesses in HR STEM can therefore easily be distinguished, even at the lower incoming electron dose of $10^4 e^-/\text{Å}^2$.

For $SrTiO_3$ also a high probability of error was found in the results presented in Fig. 2, when using PIs in HR TEM as compared to SCSs in HR STEM, for counting the number of atoms in a Sr column with a thickness up to 75 atoms. This result can now be understood since PIs oscillate for thicker crystals depending on the atomic column type, as shown in Fig. 7. This oscillating behaviour is a result of inherent electron channelling, which depends on both the atomic type and the atomic column thickness [25]. It is impossible to assign PIs in HR TEM unambiguously to a specific number of atoms when they oscillate as a function of thickness as shown in Fig. 7(a). Therefore, in the presence of noise, columns of different thickness cannot be distinguished using PIs as a performance measure, even not at relatively large electron doses. In HR STEM, however, there are no contrast oscillations at the optimal detector settings. Furthermore, the standard deviation of the PFs

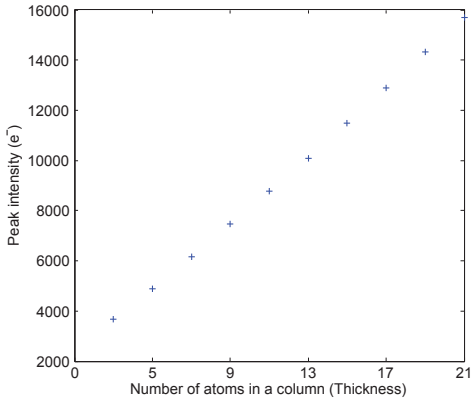

(a) PIs in HR TEM for C_s=-0.015 mm and ε = 51 Å

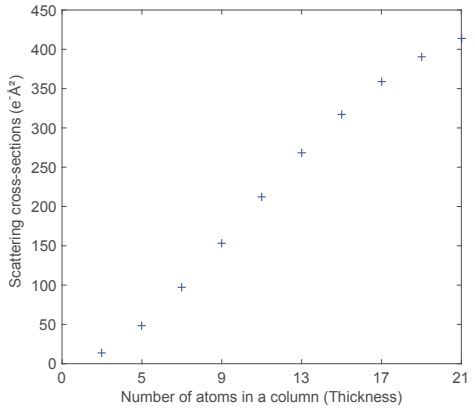

(b) SCSs in HR STEM for detector range = 13-100 mrad

Figure 5: The used performance measures for a MgO column as a function of thickness, both at the optimal experimental settings and for $N = 10^4 e^-/\text{Å}^2$.

of the SCSs in HR STEM is small as compared to the difference between the mean values of PFs of consecutive SCSs, in contrast to the PFs of PIs in HR TEM for the same incoming electron dose. As was already discussed in [9], it can be seen in Fig. 7(b) that the Low Angle Annular Dark Field (LAADF) STEM regime (21-100 mrad) is only appropriate for atom-counting up to a thickness of about 20 atoms in the column, due to the higher coherent contribution to the SCS for this detector setting. The same reasoning applies when counting the number of Au atoms.

4.2. Results for image intensities on a pixel by pixel basis

On the one hand, the results that are shown in Figs. 3 and 4 suggest that it is advantageous to use HR TEM for atom-counting, when using all image intensities on a pixel by pixel basis. In this case the probability of error for HR TEM decreases significantly as compared to the result when using PIs, and it becomes even lower than the probability of error for atom-counting in HR STEM. Note, however, that in practice the use of the joint PF of all image intensities would require a rather complex procedure. Indeed, one would then need to know the behaviour of all pixel values in the image as a function of thickness, and therefore also all imaging parameters. Recall that in the followed quantitative approach, all imaging parameters were assumed to be known exactly. Moreover, it was assumed that the spherical aberration and defocus can be tuned precisely in the case of HR TEM, which is obviously not an evident matter. In fact, the spherical aberration and defocus will be estimated parameters too, which in practice will increase the probability of error for atom-counting.

On the other hand, for atom-counting in HR STEM, it is clear from Figs. 3 and 4, that the probability of error based on the PF of the SCSs is a good approximation for the probability of error when the decision is based on the joint PF of the image pixel intensities. This is a great advantage of atom-counting using HR STEM, since SCSs are a robust measure for many imaging parameters, including defocus, source coherence, convergence angle [10], and also for crystal tilt [26].

5. Conclusions

In this paper, the limitations and possibilities for atom-counting of both HR TEM and HR STEM were investigated in a quantitative way. Three different crystals were simulated; MgO, $SrTiO_3$ and Au, in order to investigate and compare the probability of error for atom-counting in both imaging modes. By calculating the probability of error as a function of the experimental settings, the experiment design was optimised. For HR STEM, the annular inner and outer detector angles were optimised, whereas for HR TEM the spherical aberration and defocus were optimised.

We can conclude that when comparing the currently used approaches, HR STEM is in general applicable for atom-counting when using an appropriate detector range, where the SCSs monotonically increase with thickness, and where the overlap between the PFs of consecutive SCSs is small. When the atom-counting decision is based on the PF of PIs, HR TEM can only be used to count the number of atoms in projected atomic columns in a very thin sample region at optimal imaging conditions, and using a sufficiently high incoming electron dose. The PIs oscillate as a function of the thick-

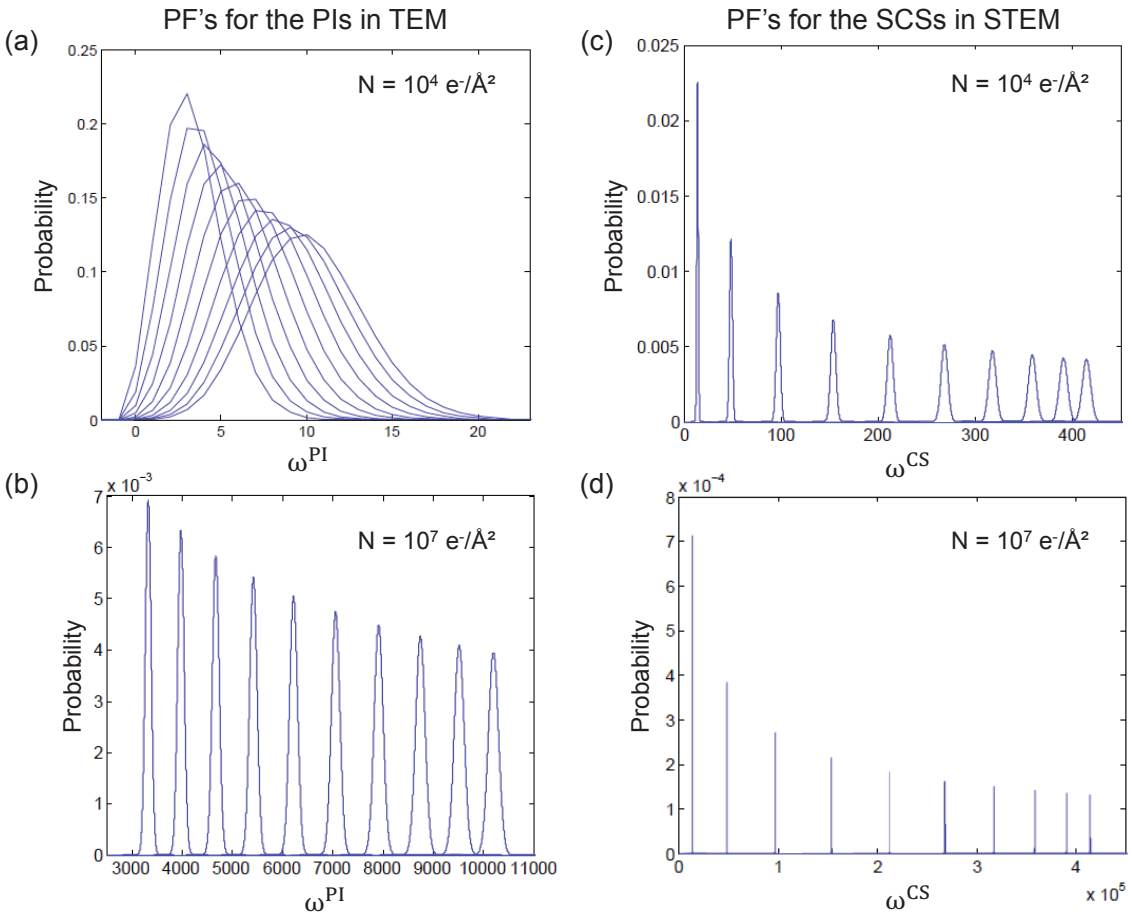

Figure 6: The PFs for the succeeding PIs in HR TEM and SCSs in HR STEM of a MgO column up to a thickness of 10 unit cells, for two different incoming electron doses.

ness, depending on the atomic column type due to the inherent electron channelling. The probability of error at the optimal experimental settings for HR TEM, when the atom-counting decision is based on the PF of PIs is larger as compared to the optimal probability of error for HR STEM, when using the same incoming electron dose. Under the assumption that one can make the atom-counting decision based on the joint PF of all image pixel intensities, the probability of error decreased significantly in the case of HR TEM, and became lower as compared to HR STEM. Note, however, that such atom-counting procedure would require the behaviour of all image pixel intensities to be known accurately as a function of thickness, which is not a trivial matter. In HR STEM, both for binary and multiple hypothesis testing, the probability of error based on the joint PF of the image pixel values is well approximated by the probability of error for SCSs, for which an appropriate and practical framework exists [1, 5, 8].

In conclusion, HRTEM may in theory result into a lower probability of error for atom-counting when using image intensities on a pixel by pixel basis, but the commonly used SCSs for atom-counting in STEM lead to a high performance and have been shown to work in practice.

6. Acknowledgements

The authors gratefully acknowledge financial support from the Research Foundation Flanders (FWO, Belgium) through project fundings (G.0368.15N, G.0369.15N, G.0374.13N, and WO.010.16N) and a postdoctoral grant to A. De Backer. The research leading to these results has received funding from

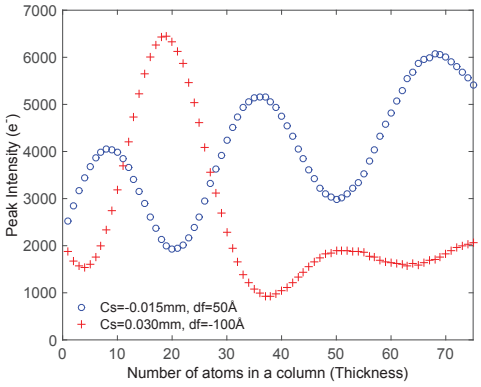

(a) PIs in HR TEM

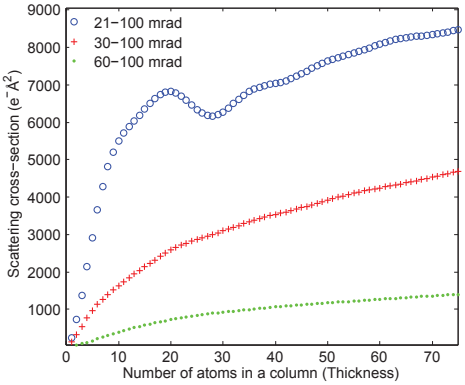

(b) SCSs in HR STEM

Figure 7: The used performance measures plotted as a function of thickness using different experimental settings for a Sr column with a thickness up to 75 atoms and $N = 10^6 e^-/\text{Å}^2$.

the European Union Seventh Framework Programme [FP7/2007-2013] under Grant agreement no. 312483 (ESTEEM2).

7. References

[1] S. Van Aert, K. J. Batenburg, M. D. Rossell, R. Erni, G. Van Tendeloo, Three-dimensional atomic imaging of crystalline nanoparticles, Nature 470 (2011) 374–377.

[2] S. Bals, M. Casavola, M. A. van Huis, S. Van Aert, K. J. Batenburg, G. Van Tendeloo, D. Vanmaekelbergh, Three-dimensional atomic imaging of colloidal core-shell nanocrystals, Nano Letters 11 (8) (2011) 3420–3424.

[3] S. Bals, S. Van Aert, C. P. Romero, K. Lauwaet, M. J. Van Bael, B. Schoeters, B. Partoens, E. Yücelen, P. Lievens, G. Van Tendeloo, Atomic scale dynamics of ultrasmall germanium clusters, Nature Communications 3 (2012) 897.

[4] P. Kundu, S. Turner, S. Van Aert, N. Ravishankar, S. Van Tendeloo, Atomic structure of quantum gold nanowires: Quantification of the lattice strain, ASC Nano 8 (2014) 599–606.

[5] S. Van Aert, A. De Backer, G. T. Martinez, B. Goris, S. Bals, G. Van Tendeloo, A. Rosenauer, Procedure to count atoms with trustworthy single-atom sensitivity, Physical Review B 87 (2013) 064107.

[6] J. M. LeBeau, S. D. Findlay, L. J. Allen, S. Stemmer, Standardless atom counting in scanning transmission electron microscopy, Nano Letters 10 (2010) 4405–4408.

[7] L. Jones, K. E. MacArthur, V. T. Fauske, A. T. J. van Helvoort, P. D. Nellist, Rapid estimation of catalyst nanoparticle morphology and atomic-coordination by high-resolution z-contrast electron microscopy, Nano Letters 14 (2014) 6336–6341.

[8] A. De Backer, G. T. Martinez, A. Rosenauer, S. Van Aert, Atom counting in HAADF STEM using a statistical model-based approach: Methodology, possibilities, and inherent limitations, Ultramicroscopy 134 (2013) 23–33.

[9] A. De Backer, A. De wael, J. Gonnissen, S. Van Aert, Optimal experimental design for nano-particle atom-counting from high-resolution STEM images, Ultramicroscopy 151 (2014) 46–55.

[10] H. E, K. E. MacArthur, T. J. Pennycook, E. Okunishi, A. J. D'Alfonso, N. R. Lugg, L. J. Allen, P. D. Nellist, Probe integrated scattering cross sections in the analysis of atomic resolution HAADF STEM images, Ultramicroscopy 133 (2013) 109–119.

[11] G. T. Martinez, A. De Backer, A. Rosenauer, J. Verbeeck, S. Van Aert, The effect of probe inaccuracies on the quantitative model-based analysis of high angle annular dark field scanning transmission electron microscopy images, Micron 63 (2014) 57–63.

[12] C. L. Jia, S. B. Mi, J. Barthel, D. W. Wang, R. E. Dunin-Borkowski, K. W. Urban, A. Thust, Determination of the 3D shape of a nanoscale crystal with atomic resolution from a single image, Nature Materials 13 (2014) 1044.

[13] A. J. den Dekker, J. Gonnissen, A. De Backer, J. Sijbers, S. Van Aert, Estimation of unknown structure parameters from high-resolution STEM images: What are the limits?, Ultramicroscopy 134 (2013) 34–43.

[14] J. Gonnissen, A. De Backer, A. J. den Dekker, G. T. Martinez, A. Rosenauer, J. Sijbers, S. Van Aert, Optimal experimental design for the detection of light atoms from high-resolution scanning transmission electron microscopy images, Applied Physics Letters 105 (063116).

[15] J. Gonnissen, A. De Backer, A. J. den Dekker, J. Sijbers, S. Van Aert, Detecting and locating light atoms from high-resolution STEM images: The quest for a single optimal design, Ultramicroscopy-doi:http://dx.doi.org/10.1016/j.ultramic.2016.07.014.

[16] J. M. LeBeau, S. D. Findlay, L. J. Allen, S. Stemmer, Quantitative atomic resolution scanning transmission electron microscopy, Physical Review Letters 100 (2008) 206101.

[17] A. Rosenauer, M. Schowalter, Stemsim - a new software tool for simulation of STEM HAADF Z-contrast imaging, in: A. G. Cullis, P. A. Midgley (Eds.), Microscopy of Semiconducting Materials 2007, Vol. 120 of Springer Proceedings in Physics, Springer Netherlands, 2008, pp. 170–172.

[18] A. Rosenauer, K. Gries, K. Müller, A. Pretorius, M. Schowalter, A. Avramescu, K. Engl, S. Lutgen, Measurement of specimen thickness and composition in $Al_xGa_{1-x}N$/GaN using high-angle annular dark field images, Ultramicroscopy 109 (2009) 1171–1182.

[19] T. Grieb, K. Müller, O. Rubel, R. Fritz, C. Gloistein, M. Schowalter, N. Neugebohrn, N. Knaub, K. Volz, A. Rosenauer, Determination of the chemical composition of GaNAs using STEM HAADF imaging and STEM strain state analysis, Ultramicroscopy 117 (2012) 15–23.

[20] I. Lobato, D. Van Dyck, MULTEM: A new multislice program to perform accurate and fast electron diffraction and imaging simulations using Graphics Processing Units with CUDA, Ul-

tramicroscopy 156 (2015) 9–17.
[21] I. Lobato, S. Van Aert, J. Verbeeck, Progress and new advances in simulating electron microscopy datasets using MULTEM, Ultramicroscopy 168 (2016) 17–27.
[22] S. M. Kay, Fundamentals of Statistical Signal Processing. Volume II Detection Theory, Prentice-Hall, Inc., New Jersey, 2009.
[23] M. De Graef, Introduction to Conventional Transmission Electron Microscopy, Cambridge Universiy Press, 2003.
[24] E. Kirkland, Advanced Computing in Electron Microscopy, Springer, 2010.
[25] P. Geuens, D. Van Dyck, The s-state model: a work horse for HRTEM, Ultramicroscopy 93 (2002) 179–198.
[26] K. E. MacArthur, A. J. D'Alfonso, D. Ozkaya, L. J. Allen, P. D. Nellist, Optimal ADF STEM imaging parameters for tilt-robust image quantification, Ultramicroscopy 156 (2015) 1–8.